Materials Science and Engineering A 540 (2012) 174–186

Contents lists available at SciVerse ScienceDirect

Materials Science and Engineering A

journal homepage: www.elsevier.com/locate/msea

Mechanical characterization and constitutive modeling of Mg alloy sheets

M. Nebebe Mekonen[a], D. Steglich[a], J. Bohlen[a], D. Letzig[a], J. Mosler[a,b,*]

[a] Helmholtz-Zentrum Geesthacht, Institute of Materials Research, D-21502 Geesthacht, Germany
[b] TU Dortmund, Institute of Mechanics, Leonhard-Euler-Str.5, D-44227 Dortmund, Germany

ARTICLE INFO

Article history:
Received 19 October 2011
Received in revised form 25 January 2012
Accepted 27 January 2012
Available online 4 February 2012

Keywords:
Mechanical characterization
Magnesium alloys
Constitutive model

ABSTRACT

In this paper, an experimental mechanical characterization of the magnesium alloys ZE10 and AZ31 is performed and a suitable constitutive model is established. The mechanical characterization is based on uniaxial tensile tests. In order to avoid poor formability at room temperature, the tests were conducted at elevated temperature (200 °C). The uniaxial tensile tests reveal sufficient ductility allowing sheet forming processes at this temperature. The differences in yield stresses and plastic strain ratios (r-values) confirm the anisotropic response of the materials under study. The constitutive model is established so that the characteristic mechanical features observed in magnesium alloys such as anisotropy and compression-tension asymmetry can be accommodated. This model is thermodynamically consistent, incorporates rate effect, is formulated based on finite strain plasticity theory and is applicable in sheet forming simulations of magnesium alloys. More precisely, a model originally proposed by Cazacu and Barlat in 2004 and later modified to account for the evolution of the material anisotropy is rewritten in a thermodynamically consistent framework. The calibrated constitutive model is shown to capture the characteristic mechanical features observed in magnesium alloy sheets.

1. Introduction

Motivated by the growing demand for light weight materials, research on magnesium and its alloys has been getting more attention. This is attributed to the fact that magnesium is the lightest metal in use for the production of structural components with a promising application in the automotive and aircraft industry. Existing applications are mainly based on cast products, whereas the utilization of semi-finished products such as sheets is to be expanded for the fabrication and application of components and structures. Despite the high strength-to-weight ratio, the application of wrought magnesium such as sheets to light weight structures is limited. However, sheets are a fundamental form of material for use in numerous industrial applications and almost every metal is also available as a sheet product which allows the production of formed components. The limitation for the structural application of magnesium sheets is correlated with its pronounced anisotropy, the compression-tension asymmetry as well as with its comparably poor formability, especially at room temperature, cf. [1–3]. A reason for this behavior is the appearance of magnesium and its alloys with a hexagonal close-packed lattice structure which limits the number of active deformation mechanisms in comparison to cubic metals. Therefore the ductility as well as the formability of magnesium sheets is limited which establishes restrictions for processing steps along the whole process chain, i.e., the rolling procedures for magnesium sheets, the forming procedures of structural components and the mechanical properties of the resulting parts.

Pursuing the objective of resolving the aforementioned limitations, recent research on magnesium focuses on two main topics. The first is the development of new magnesium alloys with improved mechanical properties and especially improved formability, see [4,5]. It was recently discovered that alloys which contain a certain amount of rare earth elements such as cerium, neodymium or yttrium, tend to develop different microstructures and especially textures during conventional rolling procedures in comparison to established standard alloys such as AZ31. It has been shown that these different microstructures and textures have a distinct impact on the sheet formability as well as on the anisotropy of mechanical properties cf. [5]. The second topic deals with the investigation of the mechanical behavior of magnesium sheet alloys as a function of the applied processing parameters in the course of component forming. In the present study, the effect of the temperature on the mechanical behavior will be addressed. The choice of testing temperatures above room temperature for the investigation is attributed to the fact that only then a reasonable formability can be achieved. A comprehensive account on this topic can be found in [6–9].

* Corresponding author at: Helmholtz-Zentrum Geesthacht, Institute of Materials Research, D-21502 Geesthacht, Germany. Tel.: +49 4152872679; fax.: +49 41528742679.
E-mail address: Joern.Mosler@HZG.de (J. Mosler).

0921-5093/$ – see front matter © 2012 Elsevier B.V. All rights reserved.
doi:10.1016/j.msea.2012.01.122

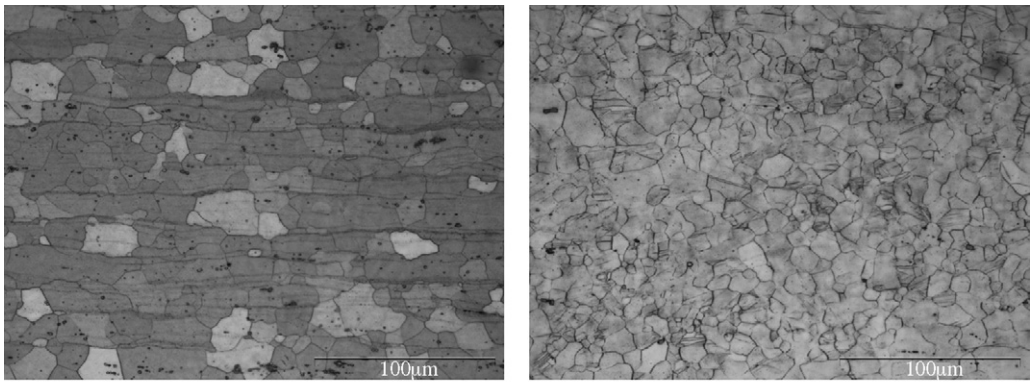

Fig. 1. Micrographs of longitudinal sections of ZE10- and AZ31-sheets in O-temper condition: both alloys show well recrystallized microstructures with comparable grain sizes. (a) ZE10. (b) AZ31.

The improvement in the formability at elevated temperatures results from the easier activation of deformation mechanisms such as prismatic slip and $\langle c+a \rangle$ pyramidal slip, cf. [10,7]. For commercial magnesium alloys, such as AZ31, the aforementioned studies indicate that sufficient formability is observed for temperatures varying between 150 °C and 250 °C. Despite the encouraging efforts made to understand the mechanical behavior of magnesium alloys at elevated temperatures, the available data on this topic are still limited. In order to supplement these limited data as well as to obtain further insight into the mechanical behavior, an experimental mechanical characterization of Mg alloy sheets is performed. The assessment of the sheet performance is often based on uni-axial mechanical testing in which strength properties, ductility, in-plane anisotropy (r-value) and strain hardening behavior are characterized. Empirical approaches for the determination of optimum forming conditions based on these data alone are not sufficient. Forming procedures such as stretch forming and deep drawing generally involve more complex loading conditions. Accordingly, there is a need for accurate simulation techniques for metal forming using the finite element (FE) analyses, which represent the current state-of-the-art in virtual prototyping, cf. [11]. For realistic finite element predictions, it is vital to use accurate plasticity models. As the quality of the prediction strongly depends on the constitutive model used, the calibration of the constitutive model parameters becomes a key issue.

Evidently, a suitable material model for numerical simulations of complex processes, such as sheet forming, should be computationally efficient. For that purpose, the so-called phenomenological constitutive models are commonly used. Over the years, several authors have proposed a number of such models describing the yielding behavior in terms of macroscopic yield functions. For instance, von Mises proposed the first yield function for anisotropic materials in the form of a quadratic function, cf. [12,11]. Later, Hill introduced a modification of this model for application to orthotropic materials with reduced parameters of anisotropy, cf. [13]. A number of alternative and versatile anisotropic models can be found in [14–16]. However, they do not capture an important feature in magnesium alloy sheets, namely the stress-differential effect. Cazacu and Barlat introduced a yield function (CaBa2004) as a modification of the Drucker model, having the capability to account for the material anisotropy as well as for the stress-differential effect, cf. [17,18]. The yield function presented in this work is based on CaBa2004. It is rewritten in tensor form employing 4th-order transformation tensors associated with the distortion of the yield locus. Even more important and different to CaBa2004, such tensors are not constant here, but evolve according to suitable evolution equations, see [19,20]. By doing so, the distortional hardening effect (change in shape of the yield locus) can be taken into account. Furthermore, in order to insure a physically sound relation, the constitutive model is recast into a thermodynamically consistent form, cf. [21–23].

2. Material characterization

2.1. Materials under investigation

Two different commercial magnesium rolled sheets have been selected for investigation: A relatively new alloy, ZE10 (Mg + 1%Zn + 0.3%Ce based mischmetal) and the well known and widely used alloy AZ31 (Mg + 3%Al + 1%Zn) in a heat treated condition (O-temper) (for detailed assessment of sheet conditions the reader is referred to [24]). Both sheets have a thickness of 1.3 mm. The differences in the mechanical behavior and the formability of the two magnesium sheet alloys have been described in earlier works, see [4,25,8]. ZE10 shows improved ductility at room temperature compared to AZ31 which is associated with an effect of the included rare earth elements and the result of deformation and recrystallization during sheet rolling. In Fig. 1 micrographs of the two sheets are presented. The grain structure is comparable between both sheets basically revealing a recrystallized microstructure corresponding to the heat treated condition of the sheets. The differences in the alloy composition lead to precipitates which can be distributed differently, e.g. in form of horizontal "stringers" in Fig. 1(a) whereas only a small number of precipitates are found for AZ31 in Fig. 1(b). It is considered that these small differences are unlikely to cause significant variations of the mechanical behavior if only the grain structure is considered. Fig. 2 shows the re-calculated (0 0 0 2) basal pole figures representing the texture of the sheets which was assessed on pole figure

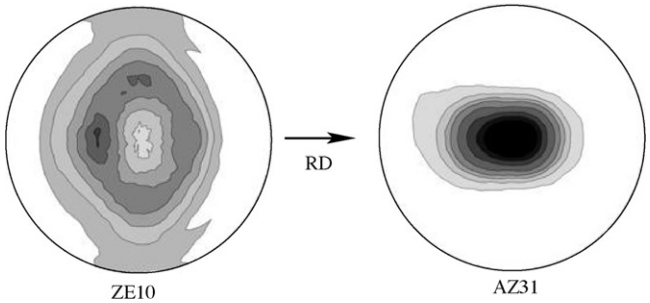

Fig. 2. Basal (0 0 0 2) pole figures of ZE10- and AZ31-sheets in O-temper condition; AZ31 shows strong basal texture, while a relatively weak texture is observed in ZE10.

measurements using a standard x-ray diffraction setup with a goniometer. The AZ31 sheet has a strong basal texture with a preferential alignment of basal planes in the sheet plane. It is understood that this preferential alignment inhibits a good ductility and formability of this sheet because basal slip as the preferred deformation mechanism is not easily activated in such orientations [4,25]. Furthermore, the angular distribution of basal planes between the normal direction (ND) of the sheet and the rolling direction (RD) is broader compared to the one between the ND and the transverse direction (TD). This favors the activation of basal slip, e.g. if stress is uni-axially applied along the RD rather than along the TD and therefore imposes a pronounced mechanical anisotropy. The ZE10 sheet exhibits a significantly weaker texture which does not exhibit the basal character which the AZ31 sheet shows. Basal planes are typically tilted away from the sheet plane, i.e., the pole figure intensity in ND is low. If it is again considered that basal slip is the preferred deformation mechanism, such orientations make it easier to activate this glide system, establishing an improved ductility and formability [6, 20]. There is still a broader distribution of basal planes toward the TD rather than toward the RD which results in an even more pronounced mechanical anisotropy in uniaxial testing. For a comprehensive description of textures in relation to the mechanical properties of materials, the reader is referred to [26].

2.2. Mechanical tests

To characterize the mechanical behavior of the magnesium sheets, uni-axial tensile tests were conducted. Specimens were prepared according to the DIN 50125-H standard. Each specimen had a gauge length of 60 mm and a width of 12.5 mm. Specimens were oriented in RD, 45° and 90° (TD) from RD, see Fig. 3(a). The tests were conducted by a universal testing machine (Zwick Z050). In order to check the reproducibility of the experimental results, at least two specimens were tested at room temperature (RT) and at an elevated temperature of 200 °C. The elevated temperature during the tests was achieved by attaching a furnace to the test machine. The choice of the test temperature 200 °C follows from the studies in [6,27]. These studies indicate that for commercial magnesium alloys such as AZ31, the forming temperature that yields sufficient formability ranges between 150 °C and 250 °C. The tests at room temperature are considered to be references based on which the tests at 200 °C are evaluated and described. For the tests conducted at RT the strain rate was set constant to 0.001/s. In order to quantify the strain rate effects at 200 °C, tests were performed at the three strain rates 0.001/s, 0.02/s and 0.1/s. For deformation measurement, mechanical extensometers in length and width direction and an optical field deformation measuring system (ARAMIS® system) were used. For the tests at RT, both systems could be used, allowing for benchmarking the optical (indirect) strain signals. Regarding the elevated temperature tests, mechanical extensometers could no longer be used due to limitations in the setup with the attached furnace. Thus, the deformation information has been solely acquired by the optical system. The use of an ARAMIS® system requires special surface treatment of the test specimens. This is necessary for establishing a stochastic pattern that can be analyzed with image processing tools. This was achieved by applying a white developer spray on the background followed by a graphite spray to create a stochastic pattern with a good contrast, see Fig. 3(b).

The mechanical responses obtained from the tensile tests are presented in terms of direction-dependent flow curves and *r*-values. The flow curves relate the true stresses with the logarithmic plastic strains. The true stress is computed from the force–displacement signal assuming material incompressibility during plastic deformation. Following the common practice, the true stresses are calculated for each test up to specimen fracture. After the onset of necking the stress state turns to be multiaxial, thus the significance of the calculated stress is limited. This is attributed in the figures by adding a shaded area to the strain interval in which strain localization (diffuse and localized necking) occurs.

Table 1
Yield stresses (YS) and ultimate tensile stresses (UTS) together with uniform (Us) and total (Ts) strain to fracture measured for ZE10 and AZ31 at RT.

Mat.	Ori.	YS (MPa)	UTS (MPa)	Us (%)	Ts (%)
ZE10	RD	144	229	11.3	16.3
	45°	121	221	15.2	22.6
	TD	111	220	15.7	18.9
AZ31	RD	163	266	18.3	21.5
	45°	175	269	16.7	20.3
	TD	187	275	16.0	17.4

The anisotropy of sheet metals can be characterized by the *r*-value defined as

$$r = \frac{\varepsilon_w^{\mathrm{pl}}}{\varepsilon_t^{\mathrm{pl}}}, \tag{1}$$

where $\varepsilon_w^{\mathrm{pl}}$ and $\varepsilon_t^{\mathrm{pl}}$ are the logarithmic plastic strains in the width and thickness direction, respectively. By assuming material incompressibility the strain $\varepsilon_t^{\mathrm{pl}}$ is calculated from the longitudinal and transverse plastic strains, i.e.,

$$\varepsilon_t^{\mathrm{pl}} = -(\varepsilon_l^{\mathrm{pl}} + \varepsilon_w^{\mathrm{pl}}) \qquad \Rightarrow \qquad r = -\frac{\varepsilon_w^{\mathrm{pl}}}{\varepsilon_l^{\mathrm{pl}} + \varepsilon_w^{\mathrm{pl}}}, \tag{2}$$

where $\varepsilon_l^{\mathrm{pl}}$ is plastic strain in the longitudinal direction. Eq. (2) is only valid for small plastic deformation or for deformation paths with a constant strain direction. Such conditions are reasonably well met for the considered experiments. The *r*-values are computed at all levels of the deformation taking advantage of the continuous measurements of the ARAMIS® system.

2.3. Results and discussion

2.3.1. Mechanical response at room temperature

The results of the tensile tests at RT are shown in Table 1 and Figs. 4 and 5. The flow curves obtained for the alloy ZE10 show higher yield stresses in RD than in TD and 45°, see Fig. 4(a). This manifests the anisotropic behavior of the material. The yield stress difference is less pronounced between TD and 45°. Represented by the shaded area, Fig. 4(a) also reveals an observable amount of localized deformation. Similar tests on AZ31 show higher yield stresses in TD than in 45°, which in turn is greater than the response in RD, see Fig. 4(b). Thus, the trend with respect to the stress level is reversed in AZ31 compared to ZE10: Whereas TD is strongest among the three orientations tested in AZ31 it is the weakest in case of ZE10. More generally, AZ31 shows a higher stress level, compare also Table 1. Although ZE10 undergoes a larger interval of localized deformation, the level of ductility for both alloys is similar.

A comparison of the *r*-values is also carried out for the two alloys. These *r*-values shown here are evaluated based on the strain measurements obtained from the ARAMIS® system. According to Fig. 5(a), the *r*-values for ZE10 at RT are below or around one. The different orientations reveal only a slight difference in *r*-values. The curves describing the *r*-values as a function of the strain show a small dependency at small strains – at strains above 0.05 the *r*-value appears to be constant.

The *r*-values for AZ31 are plotted in Fig. 5(b). From the figure, it can be seen that they are found to be strain-dependent. Although such behavior is not in line with the conventional approach of adopting a constant *r*-value, often taken within a strain range of

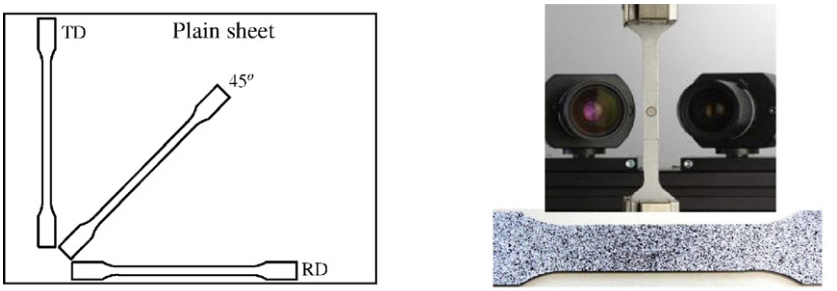

Fig. 3. Tensile test specimen configuration, experimental setup and surface treatment for ARAMIS® measurement. (a) Tensile test specimen geometry. (b) ARAMIS® setup and surface treatment.

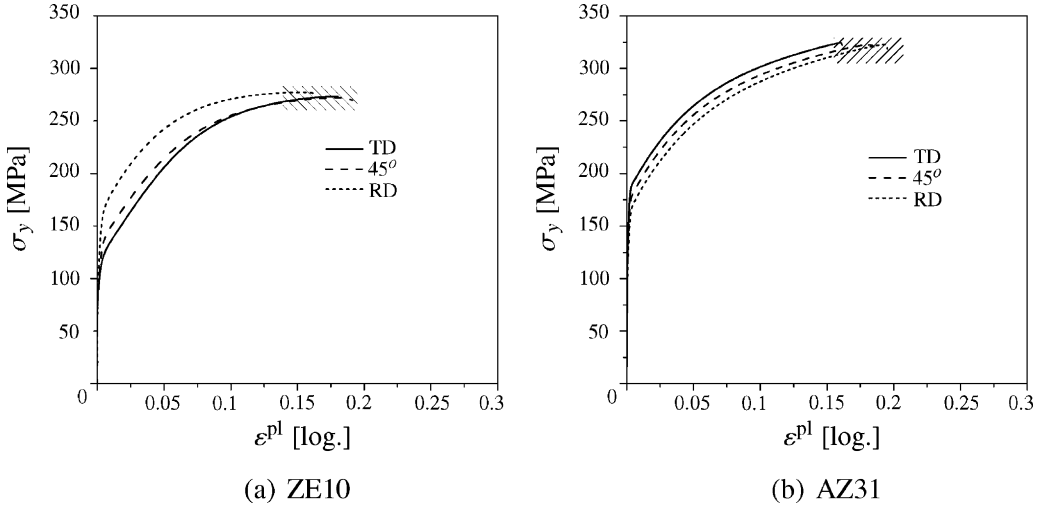

Fig. 4. Flow curves measured for ZE10 and AZ31 at room temperature; the shaded section corresponds to localized deformation. (a) ZE10. (b) AZ31.

5–20%, cf. [11,28], it is consistent with results reported in [9]. Overall, it is observed that the *r*-values of AZ31 are much higher than those of ZE10. Thus, AZ31 reveals a stronger anisotropy than ZE10 based on the *r*-values. This does not hold for the yield stresses, where ZE10 exposes a more pronounced anisotropy compared to AZ31.

2.3.2. Mechanical responses at 200 °C

The effect of temperature on the mechanical response is quantified based on equivalent uniaxial tensile tests as described above conducted at 200 °C at a constant strain rate of 0.02/s. Concerning ZE10, the first observation is a significant increase in total strain, which implies an increase in ductility, see Table 2. However, as

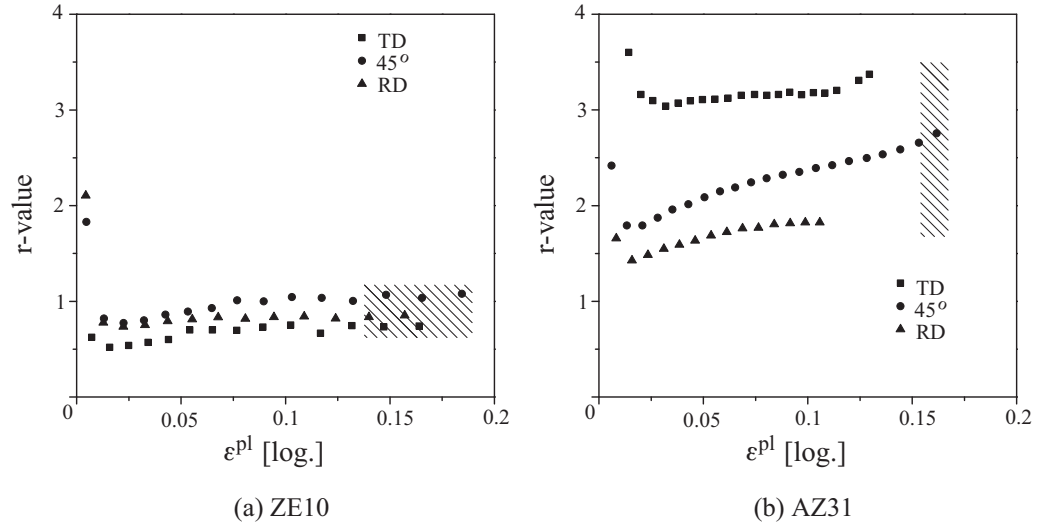

Fig. 5. *r*-values measured for ZE10 and AZ31 at room temperature; the shaded section corresponds to localized deformation. (a) ZE10. (b) AZ31.

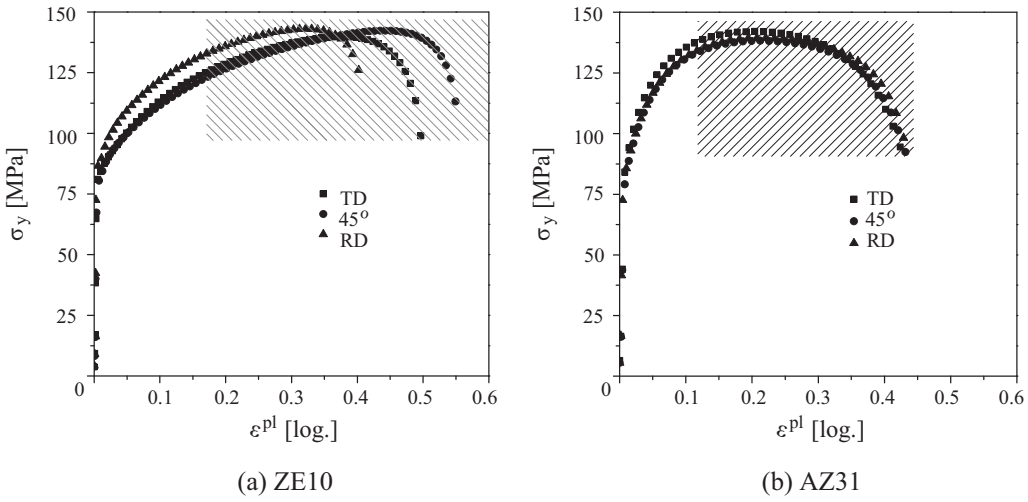

Fig. 6. Flow curves measured for ZE10 and AZ31 at 200 °C and strain rate of 0.02/s; the shaded section corresponds to localized deformation. (a) ZE10. (b) AZ31.

indicated by the shaded area in Fig. 6(a), a significant increase in localized deformation is also recorded. Another observation is a significant drop in the yield stress. It can also be seen that the yield anisotropy becomes less compared to that measured at RT. Similar observations regarding the stress–strain responses for AZ31 have also been made. A large increase in the total strain indicates an improved ductility, see Table 2. However, the uniform deformation range decreases along with the yield stress, which diminishes by more than 50% of the stress at RT. Fig. 6(b) also shows a less pronounced yield anisotropy.

From the strain measurements the *r*-values have been computed for both ZE10 and AZ31. In Fig. 7, it is shown that the *r*-values of the two alloys are influenced differently by the test temperature. The *r*-values for ZE10 show a slight increase compared to those measured at RT. Similar measurements for AZ31, however, show a decrease in *r*-values within the same strain range, see Fig. 7(b). These values show no saturation within the uniform deformation range. This suggests that the *r*-values have a stronger dependence on strain at 200 °C than at RT.

In order to quantify the strain rate effect of the analyzed alloys, additional uniaxial tensile tests at strain rates of 0.001/s and 0.1/s were conducted. The resulting effects are discussed in terms of the (representative) stress response for a specimen orientation of 45°, see Fig. 8. The figures indicate a positive strain rate dependency, i.e., the stress increases with increasing strain rate. The logarithmically scaled relation between the yield and ultimate stresses and the strain rates is depicted in Fig. 9. The effect of strain rate on ductility is quantified in Table 3. Accordingly, in the case of AZ31, the latter effect is small, whereas in the case of ZE10 the fracture strain decreases with increasing strain rate.

Fig. 10(a) for ZE10 and Fig. 10(b) for AZ31 demonstrate the effect of strain rates on the *r*-values. It is observed that, in the case of AZ31, the increase in strain rate increases the *r*-values. This also implies a considerable effect on the material anisotropy. According to the report in [9] and contrary to the above observation, the *r*-value at room temperature for AZ31 is shown to decrease with an increase in strain rate. For ZE10, although not as considerable as the increase in the case of AZ31, the increase in strain rate reduces the *r*-values.

A comparison of the stress response of differently oriented specimens under different strain rates (not shown here) revealed that the strain rate has a small effect on the material anisotropy in terms of the stress response. Thus, the rate effect on the material anisotropy can be neglected.

3. Constitutive model

Within the previous section, the magnesium alloys AZ31 and ZE10 were characterized by analyzing the mechanical response during uniaxial tension tests. According to such tests, both alloys show an anisotropic yielding behavior. Furthermore, a strain rate dependency could also be observed. However, the aforementioned findings are strictly speaking restricted to uniaxial tension tests. A convenient way of extending them to more complex stress states, e.g. those characteristic of metal forming applications, is provided by physically sound constitutive models. This is discussed in the present section. Since the focus is on the mechanical behavior prior to macroscopic damage initiation, the framework of finite strain plasticity theory is adopted.

3.1. Fundamentals of elastoplasticity at finite strains

The fundamentals of plasticity theory at finite strains as well as the used notations are briefly introduced here. A summary of the most important equations is given in Table 4. According to Table 4, the yield function, the flow rule and the evolution equations are defined with respect to the intermediate configuration. By doing

Table 2
Yield (YS) and ultimate (UTS) tensile stresses together with uniform (Us) and total (Ts) strains measured for ZE10 and AZ31 at 200 °C.

Mat.	Ori.	YS (MPa)	UTS (MPa)	Us (%)	Ts (%)
ZE10	RD	86	112	17.1	50.7
	45°	78	104	19.5	73.7
	TD	80	105	19.3	64.4
AZ31	RD	80	119	12.1	53.8
	45°	81	118	10.9	53.7
	TD	86	122	10.3	52.5

Table 3
Strain rate effect on yield stress (YS), ultimate stress (UTS), uniform strain (Us) and total strain (Ts) measured for ZE10 and AZ31 at 200 °C; orientation 45°.

Mat.	Rate	YS (MPa)	UTS (MPa)	Us (%)	Ts (%)
ZE10	0.001/s	73	91	19.4	87.6
	0.02/s	78	104	19.5	73.7
	0.1/s	81	109	18.6	61.8
AZ31	0.001/s	72	94	10.0	59.7
	0.02/s	81	118	10.9	53.7
	0.1/s	85	137	12.1	51.8

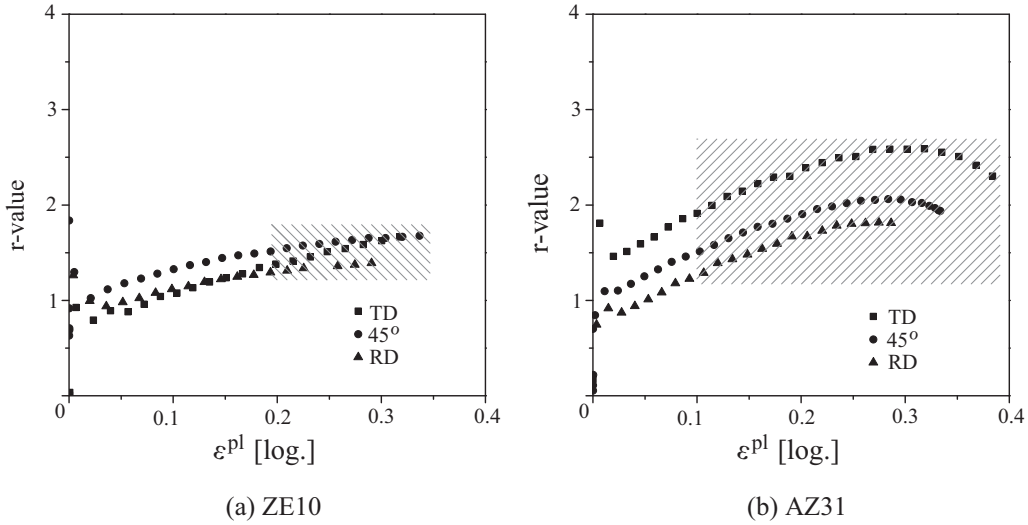

Fig. 7. *r*-values measured for ZE10 and AZ31 at 200 °C and strain rate of 0.02/s; the shaded section corresponds to localized deformation. (a) ZE10. (b) AZ31.

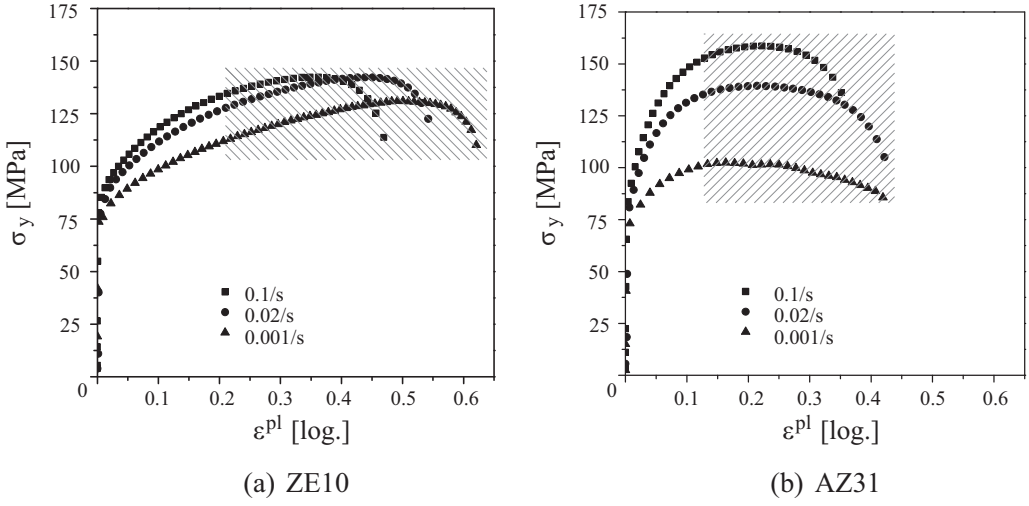

Fig. 8. Effect of strain rate on the flow curves for ZE10 and AZ31 for strain rates of 0.1/s, 0.02/s and 0.001/s at 200 °C; the shaded section corresponds to localized deformation; orientation 45°. (a) ZE10. (b) AZ31.

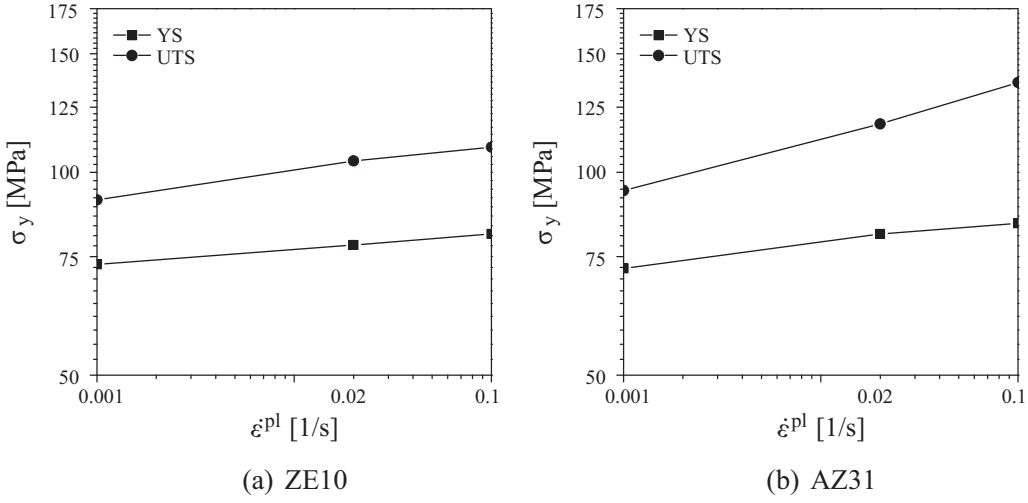

Fig. 9. Effect of strain rate on the yield (YS) and ultimate (UTS) stresses at 200 °C; orientation 45°. (a) ZE10. (b) AZ31.

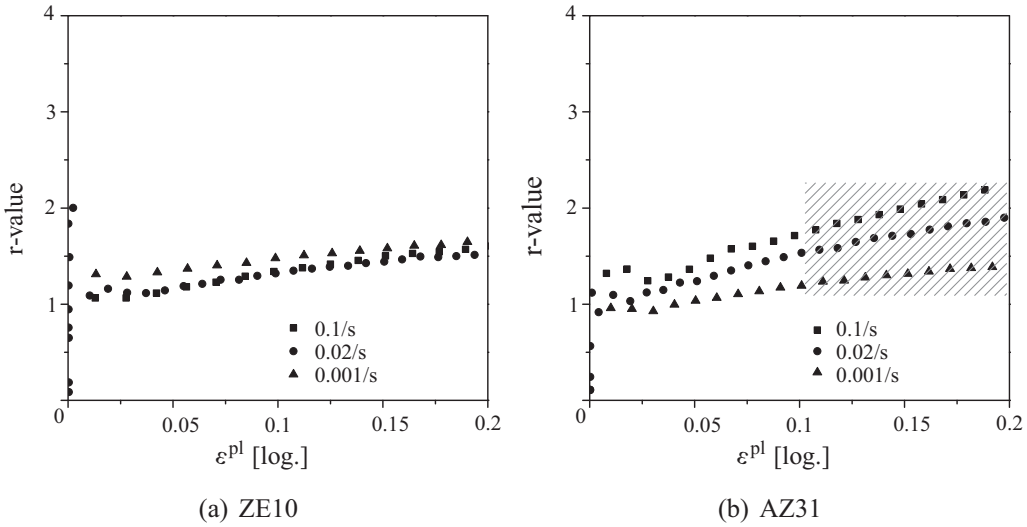

Fig. 10. Effect of strain rate on r-values for ZE10 and AZ31 for strain rates of 0.1/s, 0.02/s and 0.001/s at 200 °C; the shaded section corresponds to localized deformation; orientation 45°. (a) ZE10. (b) AZ31.

so, the principle of material frame indifference is automatically fulfilled, cf. [29].

Most equations shown in Table 4 can be applied to a broad range of different materials. A typical example is given by the multiplicative decomposition of the deformation gradient (see Eq. (30)). By way of contrast, some functions depend strongly on the material to be modeled. Those are the Helmholtz energy Ψ, the flow rule characterized by the function $\boldsymbol{M}$ (see Eq. $(33)_1$), the evolution equations defined by $\boldsymbol{g}$ (see Eq. $(33)_2$) as well as the yield function f.

Since the elastic response of magnesium is not strongly anisotropic, it can be reasonably approximated by an isotropic constitutive model. For this reason, the Neo-Hookean energy

$$\Psi^{e}(\mathbf{C}^{e}) = \frac{\lambda}{4}\left(J^{e2}-1\right) - \left(\frac{\lambda}{2}+\mu\right)\ln J^{e} + \frac{\mu}{2}\left(\mathrm{tr}\mathbf{C}^{e}-3\right) \tag{3}$$

is adopted in the present paper. Here, λ and μ represent the Lamè parameters, $J^{e} = \det \mathbf{F}^{e}$ and tr is the trace operation, cf. [30,31]. Concerning the flow rule, the normality assumption is a frequent choice. It is also adopted in the present paper implying

$$\boldsymbol{M} = \partial_{\boldsymbol{\Sigma}} f \quad \Rightarrow \quad \mathbf{L}^{pl} = \dot{\lambda}\ \partial_{\boldsymbol{\Sigma}} f. \tag{4}$$

In order to complete the constitutive model, the functions f, $\boldsymbol{g}$ and Ψ^{pl} remain to be defined. To guarantee thermodynamical consistency, they have to fulfill the reduced dissipation inequality

$$\mathcal{D} = \boldsymbol{\Sigma} : \mathbf{L}^{pl} - \dot{\Psi}^{pl} \geq 0. \tag{5}$$

Evolution equations complying with Eq. (5) will be elaborated in the following section.

3.2. A yield function describing magnesium alloys

According to Section 2, a yield function suitable for the modeling of magnesium alloys has to capture the stress differential effect. Furthermore, and in line with the underlying atomic lattice structure of the material, the yield function should only depend on the stress deviator, i.e., it should not be affected by hydrostatic stresses. A function complying with such requirements was presented in a series of papers by Cazacu and Barlat, cf. [18]. It is referred to as CaBa2004 in what follows. This function is also adopted in the present paper. However, and in sharp contrast to the cited work, the model is re-formulated in terms of Mandel stresses automatically fulfilling the principle of material frame indifference. Furthermore, it is rewritten in tensor notation here. This new notation has several advantages – particularly, for incorporating distortional hardening (distortion of the yield function). Considering perfect plasticity (no hardening), the yield function CaBa2004 reads in tensor notation

$$f = \phi(\boldsymbol{\Sigma}) - \tau_{o}^{3}, \quad \text{with} \quad \phi(\boldsymbol{\Sigma}) = \left[J_{2}^{o}(\boldsymbol{\Sigma})\right]^{\frac{3}{2}} + J_{3}^{o}(\boldsymbol{\Sigma}). \tag{6}$$

Here and henceforth, τ_{o} is the (for now constant) yield stress and $J_{2}^{o}(\boldsymbol{\Sigma})$ and $J_{3}^{o}(\boldsymbol{\Sigma})$ are the modified second and third invariants of $\boldsymbol{\Sigma}$. They are defined as

$$J_{2}^{o} = \frac{1}{2}\ \mathrm{tr}(\overline{\boldsymbol{\Sigma}}_{1}\cdot\overline{\boldsymbol{\Sigma}}_{1}) \quad \text{and} \quad J_{3}^{o} = \frac{1}{3}\ \mathrm{tr}(\overline{\boldsymbol{\Sigma}}_{2}\cdot\overline{\boldsymbol{\Sigma}}_{2}\cdot\overline{\boldsymbol{\Sigma}}_{2}), \tag{7}$$

Table 4
Fundamental equations defining rate-independent plasticity theory at finite strains. The yield function, the flow rule and the evolution equations are defined with respect to the intermediate configuration.

- Multiplicative decomposition of the deformation gradient $\mathbf{F}$ into the elastic part $\mathbf{F}^{e}$ and the plastic part $\mathbf{F}^{pl}$, cf. [38]
  $\mathbf{F} = \mathbf{F}^{e}\cdot\mathbf{F}^{pl}, \quad \text{with} \quad \det(\mathbf{F}^{e}) > 0 \text{ and } \det(\mathbf{F}^{pl}) > 0$ (30)
- Additive decomposition of the Helmholtz energy
  $\Psi = \Psi^{e}(\mathbf{C}^{e}) + \Psi^{pl}(\boldsymbol{\alpha}), \quad \text{with} \quad \mathbf{C}^{e} := \mathbf{F}^{e^{T}}\cdot\mathbf{F}^{e}$ (31)
  Here, $\boldsymbol{\alpha} \in \mathbb{R}^{n}$ is a set of internal strain-like variables associated with hardening.
- Space of admissible stresses $\mathbb{S}_{\boldsymbol{\Sigma}}$ based on a convex yield function f
  $\mathbb{S}_{\boldsymbol{\Sigma}} = \left\{ (\boldsymbol{\Sigma},\mathbf{Q}) \in \mathbb{R}^{9+n} \,\middle|\, f(\boldsymbol{\Sigma},\mathbf{Q}) \leq 0 \right\}, \quad \text{with} \quad \mathbf{Q} = -\partial_{\boldsymbol{\alpha}}\Psi^{pl}$ (32)
  $\boldsymbol{\Sigma} = 2\,\mathbf{C}^{e}\cdot\partial_{\mathbf{C}^{e}}\Psi$ denotes the Mandel stresses and $\mathbf{Q}$ is a stress-like variable conjugate to $\boldsymbol{\alpha}$.
- Flow rule and evolution equations defined by the functions $\boldsymbol{M}$ and $\boldsymbol{g}$
  $\mathbf{L}^{pl} = \dot{\mathbf{F}}^{pl}\cdot\mathbf{F}^{pl^{-1}} = \dot{\lambda}\,\boldsymbol{M}(\boldsymbol{\Sigma},\boldsymbol{\alpha}), \qquad \dot{\boldsymbol{\alpha}} = \dot{\lambda}\,\boldsymbol{g}(\boldsymbol{\Sigma},\boldsymbol{\alpha})$ (33)
  Here, $\dot{\lambda}$ denotes the plastic multiplier and the superposed dot represents the material time derivative.
- Karush–Kuhn–Tucker optimality conditions
  $\dot{\lambda} \geq 0, \quad f \leq 0, \quad \dot{\lambda} f = 0$ (34)

where stress tensors $\overline{\boldsymbol{\Sigma}}_1$ and $\overline{\boldsymbol{\Sigma}}_2$ follow from the linear transformations

$$\overline{\boldsymbol{\Sigma}}_1 = \mathbb{H}_1 : \boldsymbol{\Sigma} \quad \text{and} \quad \overline{\boldsymbol{\Sigma}}_2 = \mathbb{H}_2 : \boldsymbol{\Sigma}. \tag{8}$$

Here, $\mathbb{H}_i$ are fourth-order tensors. According to Eqs. (6)–(8) by setting $\mathbb{H}_2 = \mathbf{0}$ and $\mathbb{H}_1 = \mathbb{I} - \frac{1}{3}\ \mathbf{1}\otimes\mathbf{1}$, a von Mises-type yield function is obtained.

Although the presented constitutive model is conceptually relatively simple, the number of the respective material parameters is very large. More precisely, with $\tau_o \in \mathbb{R}$ and $\mathbb{H}_i \in \mathbb{R}^{3\times3\times3\times3}$, 163 material parameters have to be calibrated. Clearly, that is numerically and physically not practical. However, it turns out that this large number of material parameters can be significantly reduced by enforcing some physical constraints. These constraints are:

- Major symmetry: Similarly to the fourth-order elasticity tensor, $\mathbb{H}_1$ and $\mathbb{H}_2$ are assumed to show major symmetry. That is equivalent to the existence of a potential defining $\mathbb{H}_1$ and $\mathbb{H}_2$ as its Hessian.
- Minor symmetry: Since the Mandel stresses are symmetric (isotropic elastic Neo-Hookean model is used, cf. Eq. (3)), $\mathbb{H}_1$ and $\mathbb{H}_2$ show minor symmetry, i.e.,

$$\mathbb{H}_{klmn} = \mathbb{H}_{lkmn} = \mathbb{H}_{klnm} = \mathbb{H}_{mnkl} \quad \text{for} \quad \mathbb{H}_1 \quad \text{and} \quad \mathbb{H}_2. \tag{9}$$

- Pressure invariance: Since the yield function should be independent with respect to hydrostatic stress states

$$\mathbb{H}_{kkmn} = 0 \quad \text{for} \quad \mathbb{H}_1 \quad \text{and} \quad \mathbb{H}_2 \tag{10}$$

  holds.
- Orthotropic material symmetry: Magnesium sheets have an orthotropic mechanical response. In this case, the number of material parameters can be further reduced.

Combining the aforementioned physical constraints, the number of material parameters defining $\mathbb{H}_i$ can be reduced to six. Thus, using Voigt notation (matrix notation) indicated by calligraphic letters ($\mathcal{H}_i$), $\mathbb{H}_i$ can be written as six by six matrices of the type

$$\mathcal{H}_i = \begin{bmatrix} (c_2+c_3)/3 & -c_3/3 & -c_2/3 & 0 & 0 & 0 \\ -c_3/3 & (c_3+c_1)/3 & -c_1/3 & 0 & 0 & 0 \\ -c_2/3 & -c_1/3 & (c_1+c_2)/3 & 0 & 0 & 0 \\ 0 & 0 & 0 & c_4 & 0 & 0 \\ 0 & 0 & 0 & 0 & c_5 & 0 \\ 0 & 0 & 0 & 0 & 0 & c_6 \end{bmatrix} \quad i = 1, 2, \tag{11}$$

where c_j with $j = 1\ldots6$ are the reduced six components of the transformation tensors $\mathcal{H}_1$ and $\mathcal{H}_2$. For plane stress conditions, which is a reasonable assumption in most sheet forming processes, the six components of the transformation tensor can be further reduced to four. As a result, the definition of the yield function (6) requires the identification of nine parameters in this case ($dim\mathbb{H}_1 + dim\mathbb{H}_2 + dim\tau_0 = 9$).

3.3. The evolution of the yield function – hardening models

For capturing the stress–strain responses of the magnesium alloys ZE10 and AZ31, as discussed in Section 2, suitable hardening models are required. Most frequently, isotropic and kinematic hardening models are applied for that purpose. However, such models do not account for the distortion of the yield function which can also be observed for magnesium. This distortion is due to texture evolution. For incorporating this effect as well, the two transformation tensors $\mathbb{H}_i$ are considered as evolving internal variables. With this assumption, a yield function of the type

$$f = \phi(\boldsymbol{\Sigma}, \mathbb{H}_1, \mathbb{H}_2) - \tau_o^3 - [\tau(\alpha)]^3 \tag{12}$$

is considered in the present paper. Here, ϕ is defined by Eq. $(6)_2$, τ_o is the initial yield stress and τ is a stress-like internal variable associated with isotropic hardening.

According to Eq. $(32)_2$, the internal variables $\mathbf{Q} = \{\tau; \mathbb{H}_1; \mathbb{H}_2\}$ follow implicitly from the definition of the Helmholtz energy Ψ. Assuming that isotropic and the two distortional hardening mechanisms are uncoupled, yields the energy Ψ^{pl}

$$\Psi^{pl} = \Psi^{pl}_{iso}(\alpha) + \Psi^{pl}_{dist1}(\mathbb{E}_1) + \Psi^{pl}_{dist2}(\mathbb{E}_2) \tag{13}$$

with $\mathbb{E}_i$ being dual internal variables conjugate to $\mathbb{H}_i$ and α denoting the dual to τ. Concerning isotropic hardening, an exponential saturation is assumed. More precisely,

$$\tau(\alpha) = -\partial_\alpha \Psi = \Delta\tau_\infty\ [1 - \exp(\zeta\ \alpha)] \quad \Rightarrow \quad \Psi^{pl}_{iso} = \int_{\alpha=0}^{\alpha} \tau\alpha\ \mathrm{d}\alpha. \tag{14}$$

where α is the strain-like internal variable conjugate to τ, $\Delta\tau_\infty$ and ζ denote two material parameters defining the saturation value and the saturation rate of τ. The isotropic hardening model is completed by considering an associative evolution equation of the type

$$\dot{\alpha} = \dot{\lambda}\ \partial_\tau\ f. \tag{15}$$

For the sake of simplicity, quadratic functions are assumed to describe distortional hardening. Accordingly,

$$\Psi^{pl}_{disti}(\mathbb{E}_i) = \frac{1}{2}\ H_i\ \mathbb{E}_i :: \mathbb{E}_i = \frac{1}{2}\ \frac{1}{H_i}\ \mathbb{H}_i :: \mathbb{H}_i, \qquad \text{with}$$
$$\mathbb{H}_i := -\partial_{\mathbb{E}_i} \Psi^{pl}_{disti} \tag{16}$$

where H_i denotes the hardening modulus. Assuming further that distortional hardening is only driven by the internal variable α (this implies $\mathbb{E}_i = \mathbb{E}_i(\alpha)$ or equivalently $\mathbb{H}_i = \mathbb{H}_i(\alpha)$), Eq. (16) simplifies to

$$\Psi^{pl}_{disti}(\mathbb{E}_i) = \Psi^{pl}_{disti}(\alpha) \tag{17}$$

Assumption (17) is a good approximation for radial loading paths and thus complies with the experimental setup. For defining $\mathbb{H}_i$, the exponential functions

$$c_j(\alpha) = A_j + B_j(1 - \exp(-C_j\ \alpha)) \tag{18}$$

are adopted where A_j, B_j and C_j with $j = \{1\ldots6\}$ are the model parameters (for each $\mathbb{H}_i$). In line with Eq. (11), the coefficients c_j in Eq. (18) denote the components defining the tensors $\mathbb{H}_i$.

While the proposed framework automatically fulfills the principle of material frame indifference, the model parameters A_j, B_j and C_j have to be chosen in line with the second law of thermodynamics. After a straightforward calculation this law reads

$$\mathcal{D} = \boldsymbol{\Sigma} : \mathbf{L}^{pl} + \tau\ \dot{\alpha} - \dot{\Psi}^{pl}_{dist1}(\alpha) - \dot{\Psi}^{pl}_{dist2}(\alpha) \geq 0. \tag{19}$$

Here, the elastic response $\boldsymbol{\Sigma} = 2\ \mathbf{C}^e \cdot \partial_{\mathbf{C}^e}\Psi$ has already been inserted. Since the function $\phi - \tau^3$ is positively homogeneous of degree three with respect to $(\boldsymbol{\Sigma}, \tau)$, Eq. (19) can be rewritten as

$$\mathcal{D} = 3\ \dot{\lambda}\ \tau_0^3 - \dot{\Psi}^{pl}_{dist1}(\alpha) - \dot{\Psi}^{pl}_{dist2}(\alpha) \geq 0. \tag{20}$$

Evidently, the first term is greater than zero. Consequently, a sufficient condition for guaranteeing the dissipation inequality is given by

$$\mathcal{D}_{disti} := -\dot{\Psi}^{pl}_{disti}(\alpha) \geq 0. \tag{21}$$

Condition (21) which implies some restrictions on the choice of model parameters A_j, B_j and C_j is enforced within the model parameter identification described in the next section. Consequently, the resulting model fulfills the second law of thermodynamics.

Remark 1. Within the implementation, the internal variable α defined by the evolution equation

$$\dot{\alpha} = -3\ \dot{\lambda}\ \tau^2 \tag{22}$$

is replaced by the alternative choice

$$\dot{\alpha} = \sqrt{\mathbf{L}^{\mathrm{pl}} : \mathbf{L}^{\mathrm{pl}}}. \tag{23}$$

This choice is related to a previous implementation based on the classical von Mises yield function. It needs to be emphasized here that the rescaling of α implied by Eq. (23) does not essentially modify the resulting constitutive model.

Remark 2. The viscoplastic rate effect observed within the experiments is captured by replacing the rate-independent isotropic hardening variable τ (see Eq. (12)) in the yield function by its rate-dependent counterpart

$$\tau_{\mathrm{rate}} = \tau\ \left(\frac{\dot{\alpha}}{\beta}\right)^n. \tag{24}$$

Here, β and n are model parameters. According to this choice, a rate effect is only accounted for the isotropic hardening part. The shape of the yield function (distortional hardening) is thus rate-independent.

Remark 3. The implementation of the proposed constitutive model is based on the return-mapping scheme, cf. [29,32]. More precisely and following [29], the flow rule is approximated by an implicit exponential mapping and the evolution equations are integrated by employing a classical backward Euler scheme. If loading is signaled by the trial step, the root of the nonlinear set of equations (yield function, integrated evolution equations and integrated flow rule) is computed by using a Newton-Raphson scheme. Within this scheme, the plastic multiplier as well as flow direction are chosen as independent variables. Once convergence is obtained, the algorithm is linearized leading to the consistent algorithmic tangent moduli necessary for an asymptotically quadratic convergence also at the finite element level.

3.4. Summary of the constitutive model

According to the previous subsections, strain hardening in the current model consists of two parts: The distortional part expressed by transformation tensors $\mathbb{H}_i$ depending on the accumulated plastic strain α (see Eq. (18) and Eq. (11)) and an isotropic part depending on the accumulated plastic strain α and the current strain rate $\dot{\alpha}$ (see Eqs. (24) and (14)). The isotropic part naturally does not depend on the loading direction. In contrast, the distortional part allows for a strain-dependent change of the yield surfaces shape. A dependency on the strain rate in this part is not included, as experimental results indicate that material anisotropy is not significantly affected by the strain rate of the loading, see Section 2. This suggests the following sequence for the determination of the numerous model parameters. First, a reference orientation is selected and the parameters related to the isotropic rate-dependent hardening model are calibrated by tensile tests along the chosen reference direction. The stress-elongation signals are used up to their respective maximum load, thus the resulting stress states can be regarded as being uniaxial and any possible confusion with the choice of the proper equivalent measure can be avoided. Second, the parameters related to the orientation-dependent hardening tensors $\mathbb{H}_i$ are calibrated using tensile tests along different orientations while maintaining the isotropic hardening from the reference orientation. For this, the stress-elongation signal and the r-value are used. Depending on the orientation considered, the different stress levels during deformation are accounted for by the elements of the transformation tensors. This, in turn, implies that the prescribed hardening and strain rate characteristics are set by the choice of the reference orientation and will be the same for all orientations considered.

Table 5
Parameters obtained based on minimization of Eq. (25).

	$\Delta\tau_\infty$(MPa)	ζ	τ_0(MPa)	β(1/s)	n
ZE10	59.212	−8.752	87.385	2.384E−2	0.0454
AZ31	42.069	−21.147	52.140	2.185E−4	0.0841

4. Model parameter identification

The calibration of the parameters included in the constitutive model developed in Section 3 is achieved by minimizing the differences between the experimentally observed mechanical responses (see Section 2) and those predicted by the model (see Section 3). Although any experimental result can be used in general, in the following the identification procedure is limited to those data acquired for AZ31 and ZE10 at 200 °C, as the intended application of the model is the simulation of sheet metal forming operations at elevated temperatures.

4.1. Isotropic hardening including strain rate effects

The parameters related to strain hardening ($\Delta\tau_\infty$, ζ, τ_0) and those corresponding to rate effect (β, n) are computed by minimizing the target function

$$R_{\Sigma_y} = \sum_k \sum_p \left[\Sigma_{y\,kp}^{\mathrm{Exp}} - \Sigma_{y\,kp}^{\mathrm{Mod}} \right]^2 = 0 \quad , \tag{25}$$

with

$$\Sigma_y^{\mathrm{Mod}} = (\tau + \tau_0)\ \left(\frac{\dot{\alpha}}{\beta}\right)^n \quad . \tag{26}$$

The target function constitutes the differences between the experimentally measured stress responses $\Sigma_{y\,kp}^{\mathrm{Exp}}$ and the respective model predictions Σ_y^{Mod}. These differences are summed over the number of strain rate measures k (namely 0.001/s, 0.02/s and 0.1/s) and summed over a number of strain increments p (at every 0.01) along a reference orientation, the RD.

The identified parameters are presented in Table 5 for both ZE10 and AZ31. Based on the described computations at the material point level (Eq. (26) with Table 5), the uniaxial tensile test has been reanalyzed as a coupon-like structure. Thus, geometrical effects such as necking are consistently included within the resulting force–displacement. The corresponding engineering stress responses (force over undeformed cross sectional area) and those of the experiments are compared in Fig. 11.

4.2. Material anisotropy and distortional hardening

The model parameters related to distortional hardening are components of the transformation tensors $\mathbb{H}_1$ and $\mathbb{H}_2$. Each of these transformation tensors constitute the parameters A_j, B_j and C_j with $j = \{1 \ldots 6\}$. In total, this mathematical setup requires the identification of $2 \times 6 \times 3 = 36$ constants in the case of a 3D-problem. For a plane stress state, it reduces to $2 \times 4 \times 3 = 24$ constants. The identification of these parameters does not include the strain rate dependence, as experimental results indicate that material anisotropy is not significantly affected by the strain rate of the loading, see Section 2. Subsequently, the experimental results utilized

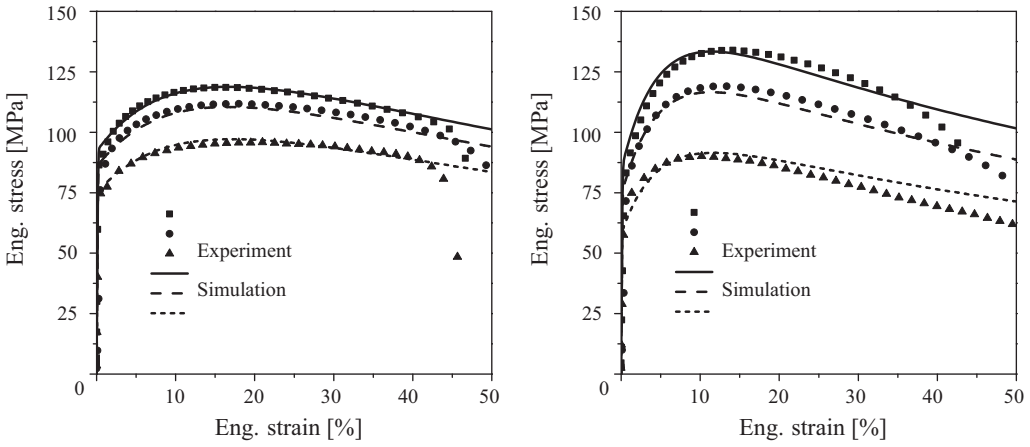

Fig. 11. Comparison between experimental and numerically predicted engineering stress responses (force over undeformed cross sectional area) for uniaxial tensile tests of ZE10 and AZ31 at strain rates of 0.1/s, 0.02/s and 0.001/s for specimens oriented in RD. (a) ZE10. (b) AZ31.

in the identification are only those obtained at 200 °C and at a strain rate of 0.02/s.

The identification of these parameters is performed through an optimization procedure. More precisely, a constrained genetic algorithm is adopted. A detailed description of such methods can be found in [33] (Section 2). The optimization method employs an objective function of the least square-type

$$\Gamma = \sum_q \sum_p \left[\mu_{qp}^{\Sigma} \left(\frac{\Sigma_{qp}^{\mathrm{Mod}}}{\Sigma_{qp}^{\mathrm{Exp}}} - 1 \right)^2 + \mu_{qp}^{r'} \left(\frac{r'^{\mathrm{Mod}}_{qp}}{r'^{\mathrm{Exp}}_{qp}} - 1 \right)^2 \right]. \quad (27)$$

This function incorporates sums accounting for stresses $\Sigma_{qp}^{()}$ as well as r-values. The sums run over the number of specimen orientations q considered during the uniaxial tensile tests and over the selected discrete points of the equivalent plastic strain p accounting for the evolution of the yield loci. μ_{qp}^{Σ} and $\mu_{qp}^{r'}$ are weighting factors to control the contribution from the stress and r-value, respectively. The superscripts Exp and Mod refer to the reference values obtained from the experiment and those related to the predictions of the model, respectively. In Eq. (27), r' is a modified r-value obtained from the ratio of the plastic strain rates. This can be approximated by the derivatives of the yield function as

$$r' = \frac{\dot{\varepsilon}_w^{\mathrm{pl}}}{\dot{\varepsilon}_t^{\mathrm{pl}}} \approx -\frac{\sin^2\theta\ \partial_{\Sigma_{xx}} f - \sin 2\theta\ \partial_{\Sigma_{xy}} f + \cos^2\theta\ \partial_{\Sigma_{yy}} f}{\partial_{\Sigma_{xx}} f + \partial_{\Sigma_{yy}} f}, \quad (28)$$

where $\dot{\varepsilon}_w^{\mathrm{pl}}$ and $\dot{\varepsilon}_t^{\mathrm{pl}}$ are the rates of the plastic strains in width and thickness direction of the tensile test specimens. The angle θ is the orientation of the tensile test specimens with respect to the rolling direction. Evidently, in the case of a constant r-value, Eq. (28) leads to the conventional r-value computed from the ratio of strains.

The optimization of the objective function in Eq. (27) is complemented by constraints imposed to ensure the validity of the identified model constants. These constraints include the convexity of the yield function, the dissipation inequality required for the thermodynamic consistency, as mentioned in Section 3.2, and non-intersecting yield loci. The different constraining conditions within the optimization scheme are implemented as follows.

First, the convexity constraint is imposed by evaluating the eigenvalues (η) of the Hessian matrix (represented by the second-order derivative of the yield function with respect to the stress tensor)

$$\det\left(\frac{\partial^2 f}{\partial \boldsymbol{\Sigma} \partial \boldsymbol{\Sigma}} - \eta \mathbb{I} \right) = 0, \quad (29)$$

for the two in-plane principal stresses at prescribed discrete strain levels and loading cases. Then the computed eigenvalues are ensured to be greater or equal to zero.

Second, the non-negative dissipation is ensured by evaluating Eq. (21) for all discrete strain and loading cases corresponding to the yield surfaces.

Finally, intersections of the yield surfaces are prevented by ensuring non-softening stress responses for all loading cases. This is achieved by computing the stress components at a given loading direction for discrete but monotonically increasing strains.

The parameters of the model are identified for both ZE10 and AZ31, see Table 6. Fig. 12 demonstrates the predicted stress responses as a function of the specimen orientations in comparison to those measured experimentally. From the figure, it can be seen that the model captures the stress response in all orientations for the specified strain range very well. Moreover, the modified r-values (r') are calculated and compared to those obtained from the experiment, see Fig. 13. The comparison shows a good agreement between the experiment and the prediction. It should also be noted that the model is capable of capturing the strain-dependency of the computed r-values. The convexity constraint imposed during the

Table 6
Parameter sets corresponding to the novel anisotropic material model.

	$\mathbb{H}_1$			$\mathbb{H}_2$		
	A	B	C	A	B	C
(a) ZE10						
c_1	−4.5	2.7	0	1.0	−5.9	6.5
c_2	−4.1	−6.5	0.1	1.2	−2.2	3.2
c_3	−3.5	−3.1	8.8	5.8	0.0	3.1
c_4	4.1	1.9	10.4	−5.4	3.4	3.9
c_5	1	0	0	0	0	0
c_6	1	0	0	0	0	0
(b) AZ31						
c_1	1.7	−1.9	0.3	2.1	−0.8	4.4
c_2	1.6	2.5	0.0	−1.5	0.6	0.8
c_3	−3.2	−2.4	3.1	0.5	2.5	1.0
c_4	1.6	1.7	2.8	−0.9	−1.2	3.3
c_5	1	0	0	0	0	0
c_6	1	0	0	0	0	0

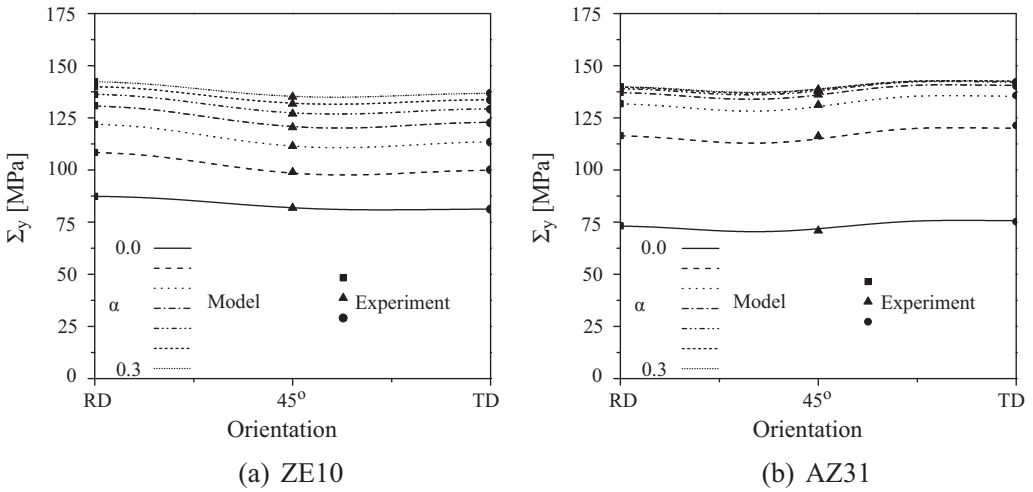

Fig. 12. Stress responses predicted by the novel anisotropic material model (see Table 6 for the material parameters) as a function of specimen orientation for strain levels ranging from 0 to 0.3 at a strain rate of 0.02/s. (a) ZE10. (b) AZ31.

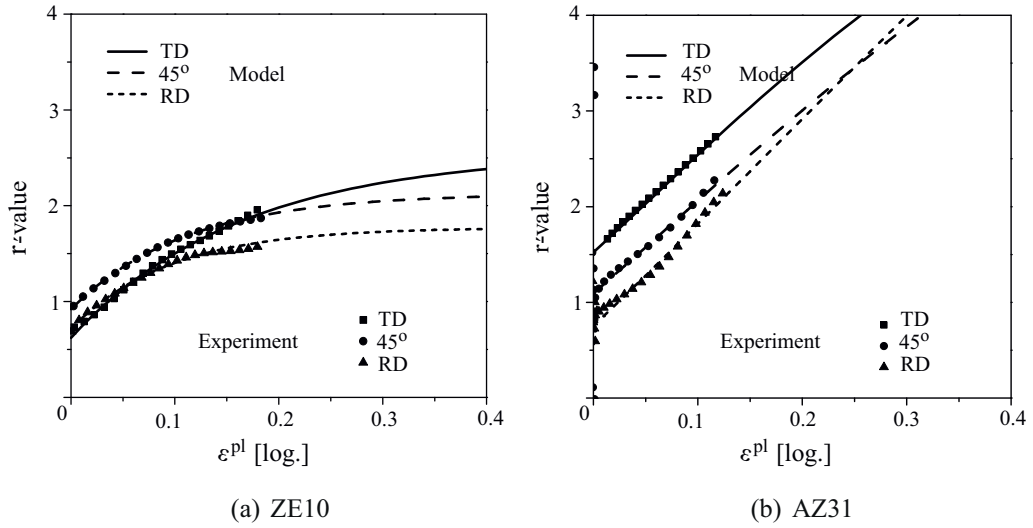

Fig. 13. r-values predicted by the novel anisotropic material model (see Table 6 for the material parameters) as a function of the plastic strain at a strain rate of 0.02/s. (a) ZE10. (b) AZ31.

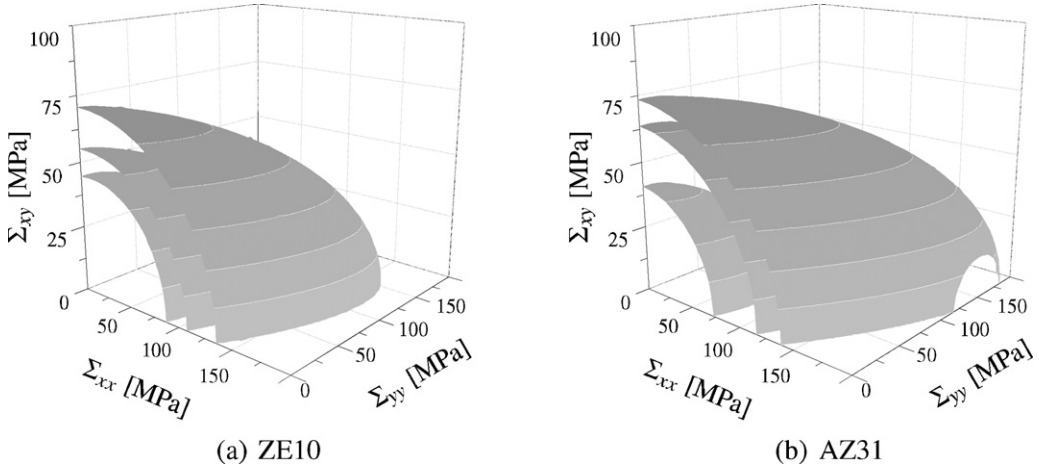

Fig. 14. Convex iso-strain contour surfaces of the stress response predicted by the novel anisotropic material model (see Table 6 for the material parameters) at a strain rate of 0.02/s. (a) ZE10. (b) AZ31.

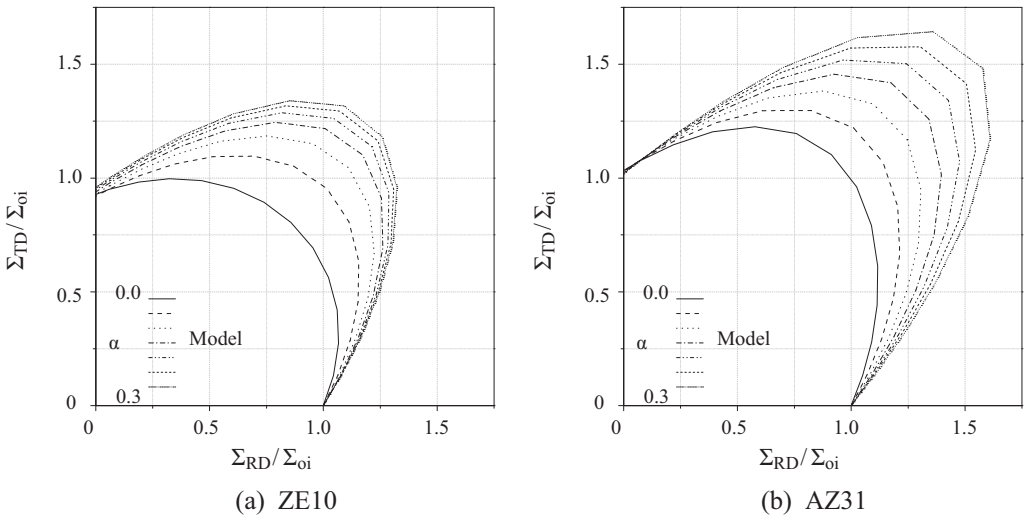

Fig. 15. Normalized iso-strain stress responses displaying the capability of the model to capture distortional hardening. (a) ZE10. (b) AZ31.

optimization procedure was indeed satisfied as shown in Fig. 14. The figure shows convex three-dimensional plots of the evolving iso-strain contours at plastic strain levels of 0.0, 0.02 and 0.1.

The feature of the model to predict a variation of the anisotropy ratio with increasing deformation directly evidences the distortional character of the calculated deformation. The change of the direction of the plastic strain increment requires a change in the yield surface shape. As mentioned previously, this is modulated by the first term in Eq. (12), which refers to the shape change. Its effect on the biaxial deformation can be illustrated by considering a two-dimensional principal stress state (plane stress, in-plane shear stresses assumed to be zero). The evolution of the yield condition, Eq. (12), with increasing plastic accumulated strain is plotted in Fig. 15(a) for ZE10 and in Fig. 15(b) for AZ31 using the identified model parameters, see Table 6. The stresses are normalized by the respective yield stress in rolling direction, Σ_{0i}, making all contours to meet at 1 on the abscissa. The respective inner contour can be regarded as an initial yield locus. While the inner contour in the case of ZE10 has a lower equi-biaxial yield stress than a uniaxial one ($\Sigma_{TD}/\Sigma_{RD} < 1$), the situation is different in the case of AZ31, where the ratio of Σ_{TD}/Σ_{RD} equals one. The subsequent contours show that hardening in the case of biaxial loading is more pronounced compared to that of uniaxial loading, which holds true for both materials. However, the effect seems to be stronger in the case of AZ31. At least for the case of AZ31 this is regarded to be in good agreement with recent findings, which quantified similar effects by either performing crystal-plasticity based FE-analysis of representative volume elements see [34] or by performing mechanical biaxial tests see [35].

5. Summary and conclusion

This paper presented the mechanical characterization of two different magnesium sheet products, together with the development of a constitutive model for numerical analyses of sheet forming processes. A calibration of the model parameters was conducted based on standard tensile tests.

The mechanical characterization was achieved through standardized uniaxial tensile tests of AZ31 and ZE10 at two test temperatures (room temperature and 200 °C), three material orientations and three loading rates. From the resulting mechanical responses an increase in ductility for higher test temperatures could be confirmed. This effect is accompanied by the expected reduction in yield stress. Furthermore, the yield stresses increased for higher strain rates showing a positive strain rate effect. The stresses depended on the loading direction: they complied with the material anisotropy as observed in tensile tests conducted at room temperature. The anisotropy was less pronounced in the case of elevated temperatures compared to room temperature. In order to analyze the anisotropy in a more detailed manner, *r*-values were computed. It was observed that they showed a strain-dependence. Based on this finding it was concluded that the materials exhibited distortional hardening. The strain-dependency of *r*-values was higher at elevated temperatures than at room temperature. Compared to ZE10, this effect is more pronounced for AZ31 due to its strong material anisotropy. The authors wish to emphasize that this has an important consequence for modeling the plastic response of the material: at elevated temperatures (where forming operations have to be performed) the distortional hardening effect has to be accounted for. It has also been observed that in the case of AZ31 the *r*-values increased with increasing strain rate, while ZE10 showed a less pronounced but opposite effect.

The large number of process parameters involved in sheet forming make experimental investigations of the process very expensive. Therefore, numerical analyses are efficient and promising substitutes. For that purpose, a novel model was developed and calibrated. This constitutive model adopts the structure of the Cazacu and Barlat 2004 model to account for the complex yielding behavior of magnesium alloys. In contrast to the Cazacu and Barlat 2004 yield function, the proposed model is frame indifferent due to the tensorial reformulation in terms of Mandel stresses. The evolution of the shape of the yield locus was accommodated by expressing the model parameters as a function of the equivalent plastic strain. Furthermore, the constitutive model was recast into a thermodynamically consistent form by imposing a non-negative dissipation.

The calibration of the model was achieved by fully utilizing the mechanical responses at 200 °C in terms of the strain-dependent *r*-values and stress responses. The reason for limiting the matrix of mechanical tests to this basic setup is obvious: reducing experimental cost and efforts. More complex experiments (e.g. hydraulic bulge and shear tests) will certainly add more physics to the model, but on the other hand make a calibration process more extensive. It was shown that the present model predicts a

pronounced increase in the equi-biaxial stress with increasing plastic strain observed by other authors. Although the generated sets of model parameters cannot be regarded as unique, the consideration of strain-dependent *r*-values provided an important information regarding the distortional hardening behavior of the investigated materials. The model has now to be assessed considering more complex loading conditions, e.g. by cup forming analyses as demonstrated in [36,37].

References

[1] E. Kelley, W. Hosford, Transactions of the Metallurgical Society of AIME 242 (1968) 654–661.
[2] W. Hosford, T. Allen, Metallurgical and Materials Transactions B 4 (1973) 1424–1425.
[3] W. Hosford, The Mechanics of Crystals and Textured Polycrystals, Oxford University Press, 1993.
[4] J. Bohlen, M. Nuernberg, J. Senn, D. Letzig, S. Agnew, Acta Materialia 55 (2007) 2101–2112.
[5] K. Hantzsche, J. Bohlen, J. Wendt, K. Kainer, S. Yi, D. Letzig, Scripta Materialia 63 (2010) 725–730.
[6] K. Dröder, Untersuchungen zum Umformen von Feinblechen ausMagnesiumknetlegierungen, Ph.D. thesis, Universität Hannover, 1999.
[7] S. Agnew, O. Duygulu, International Journal of Plasticity 21 (2005) 1161–1193.
[8] S. Yi, J. Bohlen, F. Heinemann, D. Letzig, Acta Materialia 58 (2010) 592–605.
[9] A. Khan, A. Pandey, T. Gnaeupel-Herold, R. Mishra, International Journal of Plasticity 27 (2011) 688–706.
[10] B.C. Wonsiewicz, W.A. Backofen, Transaction of Metallurgical Society of AIME 239 (1967) 1422–1433.
[11] D. Banabic, H.J. Bunge, K. Poehlandt, A.E. Tekkaya, Formability of Metallic Materials, Springer, 2000.
[12] R. von Mises, Applied Mathematics and Mechanics 592 (1928) 161–185.
[13] R. Hill, Proceeding of the Royal Society A 193 (1948) 281–297.
[14] R. Hill, Journal of the Mechanics and Physics of Solids 38 (1990) 405–417.
[15] A. Karafillis, M. Boyce, Journal of the Mechanics and Physics of Solids 41 (1993) 1859–1886.
[16] O. Cazacu, F. Barlat, Journal of Mathematics and Mechanics of Solids 6 (2001) 513–630.
[17] D. Drucker, Journal of Applied Mechanics 16 (1949) 349–357.
[18] O. Cazacu, F. Barlat, International Journal of Plasticity 20 (2004) 2027–2045.
[19] Y. Dafalias, ZAMM 59 (1979) 437–446.
[20] S. Graff, Michromechanical modeling of the deformation of HCP metals, Ph.D. thesis, Technical University of Berlin, 2007.
[21] J. Chaboche, K. Dang-Van, G. Cordier, in: Transactions of the 5th International Conference on Structural Mechanics in Reactor Technology, vol. L.
[22] Y. Dafalias, D. Schick, C. Tsakmakis, A Simple Model for Describing Yield Surface Evolution During Plastic Flow, Springer, 2003.
[23] H. Feigenbaum, Y. Dafalias, International Journal of Plasticity 20 (2004) 2027–2045.
[24] M. Avedesian, H. Baker (Eds.), ASM Speciality Handbook: Magnesium and Magnesium Alloys, ASM International, 1999.
[25] L. Stutz, D. Letzig, K. Kainer, in: K. Kainer (Ed.), Magnesium-8th International Conference on Magnesium Alloys and their Application, pp. 571–576.
[26] U. Kocks, C. Tome, H. Wenk, Texture and Anisotropy, Cambridge University Press, 1998.
[27] E. Doege, K. Dröder, Journal of Material Process Technology 117 (2001) 276–281.
[28] W. Hosford, R. Caddell, Metal Forming – Mechanics and Metallurgy, 3rd edition, Cambridge University Press, 2007.
[29] J. Simo, in: P. Ciarlet, J. Lions (Eds.), Handbook for Numerical Analysis, vol. IV, Elsevier, Amsterdam, 1998.
[30] R. Ogden, Non-linear Elastic Deformations, Dover Publications, Inc., Mineola, New York, 1984.
[31] P. Ciarlet, Mathematical Elasticity. Vol. I: Three-dimensional Elasticity, North-Holland Publishing Company, Amsterdam, 1988.
[32] J. Simo, T. Hughes, Computational Inelasticity, Springer, 1998.
[33] D. Banabic, Advanced Methods in Metal Forming, Springer, 2007.
[34] T. Hama, H. Takuda, Computational Materials Science 51 (2012) 156–164.
[35] M. Andar, D. Steglich, T. Kuwabara, in: F. Chinesta, Y. Chastel, M. Mansori (Eds.), International Conference on Advances in Materials and Processing Technologies, American Institute of Physics, 2010.
[36] D. Steglich, W. Brocks, J. Bohlen, F. Barlat, International Journal of Material Forming 4 (2011) 243–253.
[37] J. Yoon, F. Barlat, R. Dick, M. Karabin, International Journal of Plasticity 22 (2006) 174–193.
[38] E.H. Lee, D.T. Liu, Applied Physics 38 (1967) 19–27.